



Cite this: *Nanoscale*, 2021, **13**, 19165

## Controllable fabrication and photocatalytic performance of nanoscale single-layer MoSe<sub>2</sub> islands with substantial edges on an Ag(111) substrate†

Jianchen Lu,<sup>a,b</sup> Gefei Niu,<sup>b</sup> Xiao Ren,<sup>a</sup> Deliang Bao,<sup>a</sup> Hui Chen,<sup>a</sup> Haitao Yang,<sup>a</sup> Xiao Lin,<sup>a</sup> Shixuan Du<sup>a,c</sup> and Hong-Jun Gao<sup>a,c</sup>

Two-dimensional (2D) transition metal dichalcogenides (TMDs) are emerging as new electrocatalysts and photocatalysts. The edge sites of 2D TMDs show high catalytic activity and are thus favored at the catalyst surface over TMD inert basal planes. However, 2D TMDs that predominantly expose edges are thermodynamically unfavorable, limiting the number of edge sites at the surface. Herein, we demonstrate a controllable synthesis strategy of single-layer 2D MoSe<sub>2</sub> islands with a lateral size of approximately 5–12 nm on an Ag(111) substrate by pre-deposition of excess Se atoms. The surplus Se atoms react with the Ag(111) substrate and form silver selenide compounds to separate MoSe<sub>2</sub> islands and further prevent MoSe<sub>2</sub> islands from growing up. The nanoscale MoSe<sub>2</sub> islands greatly increase the ratio of exposed edge sites relative to the basal plane sites, which leads to excellent photocatalytic activity for the degradation of a methylene blue (MB) organic pollutant. This work paves the way to limit the size of 2D TMDs at the nanoscale and enables new opportunities for enhancing the catalytic activity of 2D TMD materials.

Received 27th August 2021,  
 Accepted 21st October 2021

DOI: 10.1039/d1nr05641g

rsc.li/nanoscale

### Introduction

Two-dimensional (2D) transition metal dichalcogenides (TMDs) have received considerable attention in recent years due to their remarkable properties and great potential in various fields including electronics, optics, spintronics, and catalytic devices.<sup>1–6</sup> As a member of the TMD family, single-layer molybdenum diselenide (SL-MoSe<sub>2</sub>), which has a large direct bandgap (1.5 eV),<sup>7</sup> holds promise for 2D logic devices, integrated circuits, and optoelectronics.<sup>8–11</sup>

In comparison with chemical vapor deposition (CVD) and mechanical exfoliation methods, the molecular beam epitaxy (MBE) approach has been widely utilized in obtaining SL-TMDs, owing to its advantages of controlling the quality of TMD materials at the single-atom level, which provides opportunities for precisely modulating their physical and chemical properties.<sup>12–15</sup> Ugeda *et al.* have reported that SL-MoSe<sub>2</sub> on a

bilayer graphene/6H-SiC(0001) substrate grown by the MBE method exhibits giant bandgap renormalization and an excitonic effect.<sup>16</sup> Crommie's group observed a topological state at the boundaries of 1T-WSe<sub>2</sub>, one of the quantum spin Hall insulators, grown on the bilayer graphene/6H-SiC(0001) substrate by the MBE method.<sup>17</sup>

In recent years, TMDs have been widely studied as electrocatalysts and photocatalysts in the hydrogen evolution reactions (HER),<sup>18–20</sup> oxygen reduction reactions (ORR)<sup>21,22</sup> and photocatalytic degradation of organic pollutants,<sup>23–25</sup> which make TMDs show great promise as a low-cost, stable and highly abundant alternative to traditional expensive platinum in the industry. Importantly, the edges of TMD materials are primary active sites because of their relative inertness and the poor activity of the basal plane of TMDs, which has been fully confirmed by experiments and density functional theory (DFT) calculations.<sup>19,20,26–28</sup> In addition, compared to three dimensional (3D) TMD materials, 2D TMDs manifest substantially enhanced catalytic activities. For instance, 2D SL-PtSe<sub>2</sub> demonstrates a four-time faster degradation rate than that obtained using 3D PtSe<sub>2</sub> crystals in the photodegradation of methylene blue (MB) aqueous solution.<sup>25</sup> Hence, preparation of 2D SL-TMD materials with more edge sites is one effective strategy to obtain an actual TMD-based catalyst.<sup>20,28</sup> However, due to the inherently high surface energy of edges, the controllable fabrication of 2D SL-TMD materials with exposed plentiful edges is challenging.

<sup>a</sup>Institute of Physics & University of Chinese Academy of Sciences, Chinese Academy of Sciences, Beijing 100190, P. R. China. E-mail: xlin@ucas.ac.cn, sxdu@iphy.ac.cn

<sup>b</sup>Faculty of Materials Science and Engineering, Kunming University of Science and Technology, Kunming, Yunnan 650090, P. R. China

<sup>c</sup>CAS Center for Excellence in Topological Quantum Computation, Chinese Academy of Sciences, Beijing 100190, P. R. China

†Electronic supplementary information (ESI) available. See DOI: 10.1039/d1nr05641g

In this study, we fabricated nanoscale 2D SL-MoSe<sub>2</sub> islands on an Ag(111) substrate by inducing excess selenium atoms before molybdenum atom deposition to form silver selenide compounds, limiting the growth of 2D MoSe<sub>2</sub> islands and greatly increasing the number of exposed edge sites. Atomic-scale characterization of MoSe<sub>2</sub> islands by scanning tunneling microscopy (STM) along with density functional theory (DFT) calculations and low-energy electron diffraction (LEED) and scanning tunneling spectroscopy (STS) revealed the formation of a commensurate superstructure due to the lattice mismatch between MoSe<sub>2</sub> and the Ag substrate. Raman characterization and X-ray photoelectron spectroscopy (XPS) analysis confirm the nature of SL-MoSe<sub>2</sub>. Furthermore, the photocatalytic activity of nanoscale 2D SL-MoSe<sub>2</sub> islands with a large fraction of edge sites is tested by the photocatalytic degradation of methylene blue (MB). The result shows that 2D SL-MoSe<sub>2</sub> endowed with substantial edges are a stable photocatalyst with a high photocatalytic decomposition efficiency.

## Experimental section

Sample preparation and STM characterization were performed in a standard commercial UHV LT-STM system (Omicron) with a base pressure higher than  $1 \times 10^{-10}$  mbar, equipped with standard surface processing and characterization facilities. The single-crystal Ag(111) surface (MaTeck) was cleaned by repeated cycles of 1.0 keV Ar<sup>+</sup> sputtering followed by annealing at 750 K for 30 min. The cleanliness of Ag(111) was verified by STM imaging. Molybdenum (Mo) and selenium (Se) atoms were evaporated onto the Ag surface maintained at room temperature from a commercial e-beam cell equipped with a Mo rod (99.9%, Goodfellow) and a standard Knudsen cell loaded with Se powder (99.99%, Sigma-Aldrich), respectively. To prepare nanoscale SL-MoSe<sub>2</sub> islands, Se atoms were deposited onto the Ag(111) substrate and then Mo atoms were deposited onto the Se pretreated Ag(111) substrate with a flux ratio of Mo to Se of about 1 : 10. After deposition, the substrate was post-annealed to 673 K for 30 min. Such deposition and annealing processes constitute one growth cycle. To increase the coverage of SL-MoSe<sub>2</sub> islands, the growth cycle was repeated several times. After preparation, the sample was transferred to an STM head held at 4 K. All STM images were acquired in constant current mode with an electrochemically etched tungsten tip. The sample bias is applied to the sample with respect to the tip. STS measurements were performed by using a lock-in technique with a small ac modulation signal (973 Hz, 5 mV) in another UHV STM system (Unisoku) held at 4 K. *In situ* LEED in the UHV chamber was employed to identify the superstructure macroscopically. The XPS spectra were acquired *via* an ESCALAB 250 Xi XPS microscope with ~0.1 eV resolution employing a monochromated Al K $\alpha$  X-ray source at ~1486.7 eV (~400  $\mu$ m spot size). The Raman spectra were acquired using a Renishaw spectrometer at 532 nm with about 1 mW power.

The photocatalytic activity measurement of the SL-MoSe<sub>2</sub> islands on the Ag(111) surfaces was performed by catalytic

degradation of MB molecules in an aqueous solution under visible-light irradiation at room temperature. The detailed processes are described in the literature.<sup>25</sup> The photocatalytic performance of the MoSe<sub>2</sub> islands on the Ag(111) surfaces was evaluated using a time-dependent degradation rate  $C_t/C_0$ , where  $C_t$  and  $C_0$  represent the concentrations of methylene blue molecules at time  $t$  and 0, respectively. The reaction rate of photocatalytic activity was calculated by the plots of  $\ln(C_t/C_0)$  versus irradiation time ( $t$ ) according to the pseudo-first order linear relationship, *i.e.*  $\ln \frac{C_0}{C_t} = kt$ , where  $k$  is the pseudo first order reaction rate constant ( $\text{min}^{-1}$ ).

First-principles calculations based on the density functional theory (DFT) were performed in a plane-wave formulation by the projector augmented wave (PAW) method,<sup>29</sup> as implemented in the Vienna *ab initio* simulation (VASP) package.<sup>30,31</sup> The Perdew–Burke–Ernzerhof (PBE) parameterization<sup>32</sup> of the generalized gradient approximation (GGA)<sup>33</sup> was used. Grimme's empirical correction scheme (DFT + D2) was used to take the van der Waals interaction into account.<sup>34</sup> The cutoff energy of the plane waves was 400 eV. The Brillouin zone was sampled with the  $\Gamma$ -point in all calculations. Three-layered atomic slabs were used to simulate the Ag(111) substrate, with monolayer MoSe<sub>2</sub> adsorbed on one side. The vacuum layer is 15 Å thick between neighboring slabs. In structural relaxations, the bottom layer of Ag atoms was fixed, whereas the upper two layers of Ag atoms and the monolayer MoSe<sub>2</sub> were fully relaxed until the force on every atom was smaller than 0.02 eV Å<sup>-1</sup>.

## Results and discussion

An Ag(111) single-crystal was chosen as the substrate in our work because of the silver selenide compound formation at room-temperature on the Se-pretreated Ag(111) substrate,<sup>35</sup> which provides an interesting platform for modulating the subsequent growth of the SL-MoSe<sub>2</sub> after Mo atom deposition. After two growth cycles (see the Experimental section for details), we performed STM scanning. Fig. 1a shows a typical

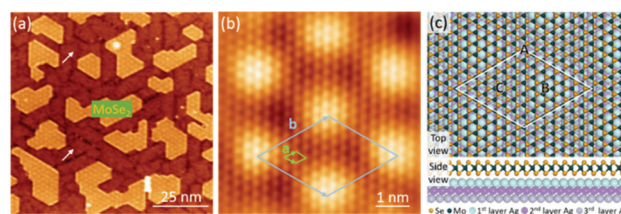


**Fig. 1** STM characterization and DFT optimized geometry of SL-MoSe<sub>2</sub> islands on the Ag(111) substrate. (a) Large-scale STM image ( $U_s = -2.5$  V and  $I_t = 0.03$  nA) of the as-prepared MoSe<sub>2</sub> on the Ag(111) substrate, showing nanoscale MoSe<sub>2</sub> islands with moiré patterns. White arrows indicate silver selenide compounds. (b) A zoom-in STM image ( $U_s = -0.01$  V and  $I_t = 8$  nA), indicating high-resolution SL-MoSe<sub>2</sub> on Ag(111). The green and blue rhombi denote the unit cell of the MoSe<sub>2</sub> lattice and the moiré patterns. (c) (Upper panel) Top view of the DFT optimized geometry of SL-MoSe<sub>2</sub> on the Ag(111) substrate and (lower panel) side view.

large-scale STM image of the as-synthesized MoSe<sub>2</sub> sample on the Ag(111) substrate. The sample terrace is partially covered by atomically flat MoSe<sub>2</sub> islands with regular moiré patterns due to the lattice mismatch between MoSe<sub>2</sub> and the Ag(111) substrate. Moreover, the moiré patterns on different islands share the same orientations, which is attributed to the good epitaxial relationship of the MoSe<sub>2</sub> islands on the Ag(111) substrate. Fig. 1b is an atomically resolved STM image, clearly exhibiting both hexagonal moiré patterns and hexagonal arrangements of the top Se atomic-layer in MoSe<sub>2</sub>, where the blue and green rhombi denote unit cells of the moiré patterns and the MoSe<sub>2</sub> lattice, respectively. The hexagonal atomic lattice of MoSe<sub>2</sub> shows a periodicity of  $\sim 3.3$  Å, which corresponds to the interatomic spacing in both basal Se and Mo planes of the SL-MoSe<sub>2</sub>. In addition, an average distance between neighboring moiré patterns is about  $\sim 23.0$  Å, which is exactly 8 times the Ag(111) lattice constant ( $a_{\text{Ag}}$ ) and 7 times the MoSe<sub>2</sub> lattice constant ( $a_{\text{MoSe}_2}$ ). Therefore, a commensurate moiré superstructure originates from the  $(7 \times 7)$  MoSe<sub>2</sub> supercells located on the  $(8 \times 8)$  Ag(111) surfaces, *i.e.*  $7 \times a_{\text{MoSe}_2}$  ( $3.29$  Å) =  $8 \times a_{\text{Ag}}$  ( $2.88$  Å) =  $a_{\text{moiré}}$  ( $23.0$  Å). The periodicities of both atomic lattices and moiré patterns are typical of SL 1H-MoSe<sub>2</sub>.<sup>15</sup>

In support of the experimental observations, we performed DFT calculations. Fig. 1c shows the optimized atomic structure of the SL-MoSe<sub>2</sub> on the Ag(111) substrate. The upper panel is a top view, showing that the orientations of the MoSe<sub>2</sub> sheet are strictly aligned with both the Ag(111) substrate and the moiré patterns. It agrees well with the experimental results, verifying the atomic model of the  $(7 \times 7)$  MoSe<sub>2</sub> on an  $(8 \times 8)$  Ag(111) substrate. The side view of the atomic model in the lower panel of Fig. 1c indicates that the height difference of the SL-MoSe<sub>2</sub> on the Ag(111) substrate is  $6.00$  Å, which indicates the van der Waals interaction between the SL-MoSe<sub>2</sub> and the Ag(111) substrate.

In order to identify the macroscopic superstructure, we performed the *in situ* LEED measurement for the as-prepared SL-MoSe<sub>2</sub> on the Ag(111) substrate. Fig. S1a† is a typical LEED pattern, where six outer bright spots marked by blue cycles can be assigned to the pristine six-fold symmetry of the Ag(111) substrate and six inner spots marked by yellow cycles belong to the SL-MoSe<sub>2</sub>. The red dashed line in Fig. S1a† indicates a parallel alignment between the SL-MoSe<sub>2</sub> and the Ag(111) substrate, suggesting the same orientation of two lattices, which fits well with the experimental and DFT calculated results. More importantly, individual LEED patterns obtained at different locations across the whole sample remain unchanged, which indicates the formation of highly ordered single-crystalline SL-MoSe<sub>2</sub> on the Ag(111) substrate.

To further confirm the formation of the SL-MoSe<sub>2</sub> on the Ag(111) substrate, we performed Raman characterization. Fig. 2a depicts a typical Raman spectrum of a MoSe<sub>2</sub>/Ag(111) sample. Two characteristic Raman modes are clearly identified, A<sub>1g</sub> mode (out-of-plane vibration) at low wavenumbers ( $242.0$  cm<sup>-1</sup>) and E<sub>2g</sub><sup>1</sup> mode (in-plane vibration) at high wavenumbers ( $287.1$  cm<sup>-1</sup>). According to previous studies on

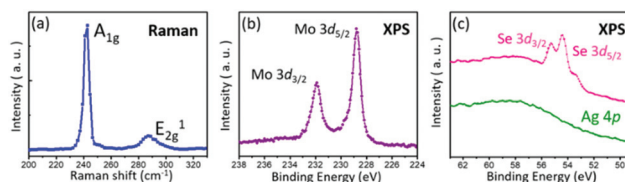


**Fig. 2** Raman spectrum and core-level XPS spectra of the SL-MoSe<sub>2</sub> on the Ag(111) substrate. (a) Raman spectrum of SL-MoSe<sub>2</sub> islands on the Ag(111) substrate. The dominant Raman features of A<sub>1g</sub> and E<sub>2g</sub><sup>1</sup> are visible with peak positions at  $242.0$  cm<sup>-1</sup> and  $287.1$  cm<sup>-1</sup>, respectively. (b and c) XPS spectra show the Mo 3d peaks with peak positions at  $231.9$  eV (3d<sub>3/2</sub>) and  $228.8$  eV (3d<sub>5/2</sub>), and the Se 3d peaks with peak positions at  $55.2$  eV (3d<sub>3/2</sub>) and  $54.4$  eV (3d<sub>5/2</sub>). The down panel of (c) presents the Ag 4p XPS signal of pure Ag(111).

mechanically exfoliated SL-MoSe<sub>2</sub> on SiO<sub>2</sub>/Si substrates,<sup>7,36–38</sup> these two typical Raman modes obtained in our sample demonstrate that the SL-MoSe<sub>2</sub> has been successfully synthesized. Chemical compositions and bonding features of the SL-MoSe<sub>2</sub> on the Ag(111) substrate were examined by XPS, as shown in Fig. 2b and c. Mo 3d<sub>3/2</sub> and 3d<sub>5/2</sub> core level peaks (Fig. 2b) are located at  $\sim 231.9$  and  $\sim 228.8$  eV, respectively, revealing the Mo(+4) chemical state, while Se 3d<sub>3/2</sub> and 3d<sub>5/2</sub> (Fig. 2c) are located at  $\sim 55.2$  and  $54.4$  eV, which indicates the  $-2$  oxidation chemical state of Se. Moreover, an intensity uplift in the XPS spectrum is observed for the Se 3d core level from a lower to a higher binding energy. This can be attributed to the contribution of the Ag 4p core level (green curve in Fig. 2c) from the Ag(111) substrate. For clarity, we subtract the XPS spectrum of the Ag 4p core level from the spectrum of the Se 3d core level and fit well with two peaks (Se 3d<sub>3/2</sub> and 3d<sub>5/2</sub>), as shown in Fig. S2,† indicating a single chemical state of Se<sup>2-</sup> in our sample. Moreover, the AgSe monolayer also exists on the Ag(111) substrate. According to the Se XPS spectrum of the AgSe monolayer on the Ag(111) substrate,<sup>35</sup> the Se element in the AgSe monolayer is also close to a  $-2$  chemical state and will share almost the same energy positions with the Se element in the SL-MoSe<sub>2</sub>.

To explore the electronic properties of the SL-MoSe<sub>2</sub>, we measured and mapped the local density of states (LDOS) by using STS. Fig. 3a shows three typical STS spectra obtained on three distinct domains in one moiré pattern marked as A, B and C, as shown in the inset STM image. All the three spectra denote a semiconducting bandgap signature of the SL-MoSe<sub>2</sub> on the Ag(111) substrate. The valence band maximum (VBM) locates at  $-1.51$  eV and the conduction band minimum (CBM) locates at  $0.36$  eV. Therefore, our STS measurements yield an electronic bandgap of  $E_g = E_{\text{CBM}} - E_{\text{VBM}} = 1.87$  eV, which is in good agreement with previous reports.<sup>15</sup> Furthermore, the main difference between the three distinct domains in STS spectra focuses on the intensities of the valence band and the conduction band. In order to demonstrate the difference of the electronic state more clearly, we developed dI/dV maps for the three domains. Fig. 3c and d show two representative dI/dV maps measured at the occupied state of  $-1.9$  V and the unoccupied state of  $0.9$  V, respectively. Fig. 3b is the corresponding

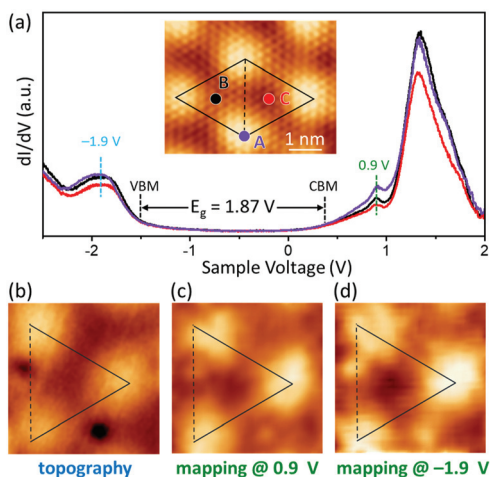


**Fig. 3** Electronic properties of the SL-MoSe<sub>2</sub> on the Ag(111) substrate. (a) Typical  $dI/dV$  spectra of the SL-MoSe<sub>2</sub> taken on three distinct domains marked with the dots of the inset STM image ( $U_s = -0.01$  V and  $I_t = 5$  nA). (b) A topography STM image ( $3.5$  nm  $\times$   $3.5$  nm,  $U_s = -1.5$  V and  $I_t = 0.1$  nA) of MoSe<sub>2</sub> with three moiré dots. (c) and (d)  $dI/dV$  mapping images acquired at  $0.9$  eV (c) and  $-1.9$  eV (d).

topography image overlaid with a triangle, indicating the half of one unit cell of the moiré pattern. For the maps at  $0.9$  eV (Fig. 3c) and at  $-1.9$  eV (Fig. 3d), the spatial distribution of the STS signals is quite similar to the related topography image (Fig. 3b), indicating that the LDOS in the SL-MoSe<sub>2</sub> is dominantly modulated by moiré patterns.

In addition, we also performed STS measurements on the edge of SL-MoSe<sub>2</sub> islands on the Ag(111) substrate. The result shows that the STS curves collected from the three longer edges of a MoSe<sub>2</sub> island have the same variation trend with the curves measured on the longer edges of SL-MoSe<sub>2</sub> islands on an Au(111) substrate (see Fig. S3† for more details).<sup>15</sup>

The nanoscale SL-MoSe<sub>2</sub> islands on the Ag(111) substrate have excellent thermal stability. As shown in Fig. S4† after annealing to  $450$  °C for  $30$  min, the nanoscale SL-MoSe<sub>2</sub> islands still maintain their original structures. In addition, the nanoscale SL-MoSe<sub>2</sub> islands are also stable under ambient conditions at room temperature (see Fig. S4† for more details).

Besides the regular MoSe<sub>2</sub> islands, the dark red colored features (white arrows in Fig. 1a and Fig. S5a†) are the silver selenide compounds formed by excessive Se atoms on the bare Ag(111) substrate. The compounds have two different apparent structures. One has a moiré periodicity of  $2.54$  nm, as shown in Fig. 4a and S5,† which had been confirmed to be an AgSe monolayer on the Ag(111) substrate.<sup>35</sup> The other is an unknown  $3 \times 3$  superstructure with respect to the Ag(111) substrate. Fig. S5e† shows a highly resolved STM image of the  $3 \times 3$  superstructure. The existence of the AgSe monolayer and the  $3 \times 3$  superstructure has also been confirmed by the LEED characterization (Fig. S1†) (see ESI† for detailed analysis).

Due to the formation of silver selenide compounds on the bare Ag(111) substrate prior to Mo deposition,<sup>35</sup> the subsequently formed SL-MoSe<sub>2</sub> islands are hard to migrate and

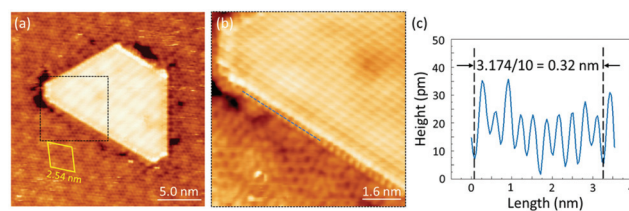


**Fig. 4** Edge terminations of nanoscale SL-MoSe<sub>2</sub> islands on the Ag(111) substrate. (a) STM image of an isolated SL-MoSe<sub>2</sub> island with alternate longer edges and shorter edges. The rest of the region is the AgSe monolayer. A rhombus denotes the moiré pattern with a periodicity of  $2.54$  nm. ( $U_s = -0.01$  V and  $I_t = 3$  nA) (b) Highly resolved STM image of one SL-MoSe<sub>2</sub> edge. ( $U_s = -0.01$  V and  $I_t = 8$  nA) (c) Line-profile along the dashed black line in (b), showing that the periodicity of rodlike protrusions is  $3.2$  Å.

ripen during the post-annealing process. Fig. 5a and b show the STM images of the as-synthesized SL-MoSe<sub>2</sub> islands on the Ag(111) substrate after one growth cycle and two growth cycles, respectively, where calculated coverages of SL-MoSe<sub>2</sub> islands are  $0.17$  and  $0.38$  ML, respectively. A statistical analysis of the size distribution (averaged lateral length of each island) of SL-MoSe<sub>2</sub> islands depicts that the predominant average size is  $5$ – $9$  nm and  $9$ – $12$  nm for one growth cycle and two growth cycles, respectively, as shown in Fig. 5c and d. Although the coverages of SL-MoSe<sub>2</sub> islands can reach about  $1$  ML by repeating the growth cycles several times and the SL-MoSe<sub>2</sub> islands can connect together in most regions, holes with various sizes composed of silver selenide compounds exist in the interior of the SL-MoSe<sub>2</sub> islands, as shown in Fig. S6.†

Compared to the SL-MoSe<sub>2</sub> islands grown on an Au(111) substrate in the similar coverage,<sup>15</sup> the statistical average size of MoSe<sub>2</sub> islands on the Ag(111) substrate is much smaller, confirming that a size-controlled epitaxy of MoSe<sub>2</sub> islands with a nanoscale size was achieved through the pre-formation of

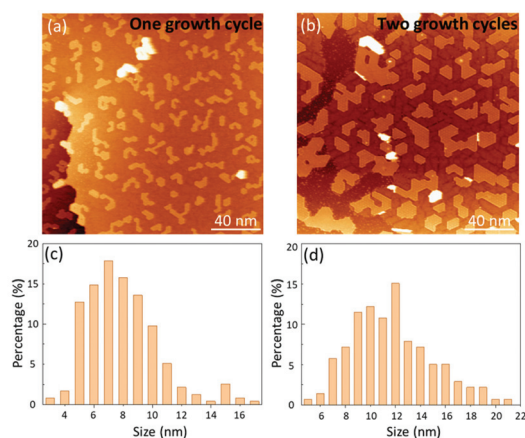


**Fig. 5** The growth of nanoscale SL-MoSe<sub>2</sub> islands on the Ag(111) substrate. (a) and (b) Large-scale STM images of SL-MoSe<sub>2</sub> islands after one growth cycle and two growth cycles. (a) ( $U_s = -2.5$  V and  $I_t = 0.03$  nA) and (b) ( $U_s = -2.5$  V and  $I_t = 0.03$  nA). (c) and (d) Size distributions (averaged lateral length) of SL-MoSe<sub>2</sub> islands after one growth cycle and two growth cycles by counting hundreds of MoSe<sub>2</sub> islands.

silver selenides on the Ag(111) substrate. It is worth noting that in the same coverage, the smaller the size of the MoSe<sub>2</sub> islands, the larger the proportion of the exposed edge sites. More edges in the SL-MoSe<sub>2</sub> islands will give rise to a better photocatalytic activity,<sup>19,20</sup> which will be verified later in a photocatalytic experiment.

Fig. 4a shows an isolated SL-MoSe<sub>2</sub> island with alternate longer edges and shorter edges. Fig. 4b is a zoom-in atomically resolved STM image of edges, which presents regular arrays of rodlike protrusions. The distance between two protrusions is about 3.2 Å in the longer edge according to the line profile shown in Fig. 4c, which is in good agreement with that in the longer edge of SL-MoSe<sub>2</sub> islands on the Au(111) substrate.<sup>15</sup> We then predict that the as-synthesized SL-MoSe<sub>2</sub> islands on the Ag(111) substrate are preferentially terminated by Mo edges with single Se atoms saturated in longer ones and bare Se edges in shorter ones. Importantly, the preferentially exposed Mo edges on the MoSe<sub>2</sub> islands are experimentally confirmed to be the active sites in the catalytic reaction.<sup>19</sup>

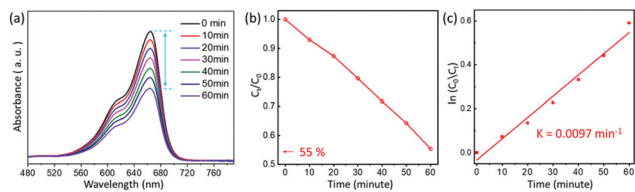
The edges of 2D TMD materials are considered to be major active sites, showing higher photocatalytic performance, as predicted and experimentally verified in previous studies.<sup>19,20,26–28</sup> Motivated by the above fact, we evaluated the photocatalytic activity of the synthesized SL-MoSe<sub>2</sub> islands featuring a large number of edges by the degradation of an MB solution under visible light irradiation. The initial concentration of the MB solution was 0.5 mg L<sup>-1</sup>. Before light irradiation, the MB solution within the MoSe<sub>2</sub>/Ag(111) sample was maintained in darkness for 1 hour to build up the sorption equilibrium. The visible light source was provided by a 150 W Xe lamp and five milliliters of the MB solution was withdrawn every 10 min of illumination and 6 sets of data were selected. Meanwhile, the concentration of MB molecules was determined by monitoring their characteristic adsorption peak at 667 nm.

Fig. 6a shows the photodecomposition of MB solution by MoSe<sub>2</sub> islands on the Ag(111) substrate under visible light irradiation. The concentration of MB decreases with the irradiation time gradually from 0 min to 60 min, indicating the visible light driven catalytic decomposition of the MB solution. The photodegradation degree of the MB solution as a

function of time is shown as the red curve in Fig. 6b. It clearly demonstrates that the degradation percentage increases with the irradiation time. After 60 min of visible light irradiation, about 45% of MB molecules can be degraded (55% of MB molecules leave behind). Furthermore, according to the pseudo-first order kinetic model,  $\ln \frac{C_0}{C_t} = kt$ , where  $k$  is the pseudo first order reaction rate constant (min<sup>-1</sup>), we calculated the kinetic photodegradation curves (Fig. 6c). The calculated reaction rate constants can reach 0.0097 min<sup>-1</sup> for nanoscale MoSe<sub>2</sub> islands. The apparent rate constant is almost 6 times that of pure MoSe<sub>2</sub> bulk materials,<sup>39</sup> putting nanoscale MoSe<sub>2</sub> islands in the same class as vertically oriented ultrathin MoSe<sub>2</sub> nanosheets and flower-like MoSe<sub>2</sub> microspheres.<sup>39,40</sup> The higher photocatalytic activities for SL-MoSe<sub>2</sub> islands with the size of several nanometers on the Ag(111) substrate confirms that the exposed edge sites in the MoSe<sub>2</sub> islands can really improve the photocatalytic performance.

The possible photocatalytic degradation mechanism for nanoscale single-layer MoSe<sub>2</sub> islands on the Ag(111) substrate is as follows: when visible light was irradiated on the surface of nanoscale single-layer MoSe<sub>2</sub> islands, the electron ( $e_{CB}^-$ ) was excited from the valence band into the conduction band, leaving the hole in the valence band ( $h_{VB}^+$ ). Such photoexcited electrons and holes will react with dissolved oxygen and H<sub>2</sub>O to generate active superoxide  $\cdot O_2^-$  and  $\cdot OH$  radicals, which degrade the adsorbed MB pollutants into CO<sub>2</sub> and H<sub>2</sub>O.<sup>23,41,42</sup> According to the previous studies, the  $\cdot OH$  radicals are the main active species in the photocatalysis process.<sup>43</sup>

The photocatalytic activity of nanoscale SL-MoSe<sub>2</sub> islands with abundant edges on the Ag(111) substrate is compared to SL-MoSe<sub>2</sub> with fewer edges on the Al<sub>2</sub>O<sub>3</sub> substrate by the degradation of MB solution under visible light irradiation. The result unambiguously confirms that the nanoscale SL-MoSe<sub>2</sub> islands featuring more edges have a higher photocatalytic activity (see Fig. S7 and S8† for more details). The as-formed nanoscale single-layer MoSe<sub>2</sub> islands on the Ag(111) substrate exhibit multiple merits for the improved photocatalytic activity. (1) MoSe<sub>2</sub> edges have been found to dramatically enhance the photocatalysis, benefitting from the metallicity of edges<sup>15</sup> and thus better electrical conductivity. (2) The abundant active edge sites of nanoscale MoSe<sub>2</sub> islands on the Ag(111) substrate will greatly improve the adsorption ability of dye organic pollutants. (3) Owing to the interfacial interaction between the single-layer MoSe<sub>2</sub> islands and the Ag(111) substrate, the photo-generated electrons will be easy to transfer from the MoSe<sub>2</sub> islands onto the Ag(111) surface, which will reduce the recombination rate of electrons and holes.<sup>39</sup>



**Fig. 6** Photocatalytic activity of nanoscale SL-MoSe<sub>2</sub> islands on the Ag(111) substrate. (a) Photodecomposition of MB solution by SL-MoSe<sub>2</sub> islands on the Ag(111) substrate under visible light irradiation. The blue two-headed arrows indicate the total decrease of the MB concentration from 0 min to 60 min. (b) Normalized concentration of MB solution vs. time.  $C_t$  and  $C_0$  are the MB concentrations at the light irradiation time  $t$  min and 0 min, respectively. (c) Kinetic photodegradation curves for the MB solution.

## Conclusions

In conclusion, we successfully synthesized nanoscale 2D SL-MoSe<sub>2</sub> islands on the Ag(111) substrate by pre-depositing excess Se atoms. STM, LEED, XPS, and Raman characterization along with DFT calculations reveal the atomic structures and

single-layer nature of 2D MoSe<sub>2</sub> islands. The nanoscale MoSe<sub>2</sub> islands possess substantial catalytically active edge sites, which was verified experimentally by the excellent visible-light-driven photocatalytic degradation of MB organic pollutants. The successful construction of 2D SL-MoSe<sub>2</sub> endowed with a large number of active edge sites may pave the way towards the production of more 2D TMD based efficient photocatalysts for environmental engineering applications.

## Author contributions

H.-J.G., S.X.D. and X.L. conceived and coordinated the research project. J.C.L. and H.C. performed the growth and STM measurements. D.L.B. carried out theoretical calculations. X.R. and H.T.Y. performed the photocatalytic experiments. J.C.L. and G.F.N. drafted and edited the manuscript. All authors participated in the discussion of the data.

## Conflicts of interest

There are no conflicts to declare.

## Acknowledgements

This work was supported by the National Key Research and Development Projects of China (2018YFA0305800 and 2019YFA0308500), the National Natural Science Foundation of China (61901200, 61925111, and 61888102), the Strategic Priority Research Program of Chinese Academy of Sciences (XDB30000000), the Yunnan Fundamental Research Projects (2019FD041 and 202101AW070010), and the Analysis and Testing Fund of KUST (2020M20192230154).

## References

- 1 B. Radisavljevic, A. Radenovic, J. Brivio, V. Giacometti and A. Kis, *Nat. Nanotechnol.*, 2011, **6**, 147–150.
- 2 D. Xiao, G. B. Liu, W. X. Feng, X. D. Xu and W. Yao, *Phys. Rev. Lett.*, 2012, **108**, 196802.
- 3 Q. H. Wang, K. Kalantar-Zadeh, A. Kis, J. N. Coleman and M. S. Strano, *Nat. Nanotechnol.*, 2012, **7**, 699–712.
- 4 Z. R. Gong, G. B. Liu, H. Y. Yu, D. Xiao, X. D. Cui, X. D. Xu and W. Yao, *Nat. Commun.*, 2013, **4**, 1–6.
- 5 X. D. Xu, W. Yao, D. Xiao and T. F. Heinz, *Nat. Phys.*, 2014, **10**, 343–350.
- 6 R. Kappera, D. Voiry, S. E. Yalcin, B. Branch, G. Gupta, A. D. Mohite and M. Chhowalla, *Nat. Mater.*, 2014, **13**, 1128–1134.
- 7 S. Tongay, J. Zhou, C. Ataca, K. Lo, T. S. Matthews, J. Li, J. C. Grossman and J. Wu, *Nano Lett.*, 2012, **12**, 5576–5580.
- 8 Q. H. Wang, K. Kalantar-Zadeh, A. Kis, J. N. Coleman and M. S. Strano, *Nat. Nanotechnol.*, 2012, **7**, 699–712.
- 9 D. Jariwala, V. K. Sangwan, L. J. Lauhon, T. J. Marks and M. C. Hersam, *ACS Nano*, 2014, **8**, 1102–1120.
- 10 K. F. Mak and J. Shan, *Nat. Photonics*, 2016, **10**, 216–226.
- 11 X. Qian, J. Liu, L. Fu and J. Li, *Science*, 2014, **346**, 1344–1347.
- 12 G. Li, Y. Y. Zhang, H. Guo, L. Huang, H. Lu, X. Lin, Y. L. Wang, S. Du and H. J. Gao, *Chem. Soc. Rev.*, 2018, **47**, 6073–6100.
- 13 X. Lin, J. C. Lu, Y. Shao, Y. Y. Zhang, X. Wu, J. B. Pan, L. Gao, S. Y. Zhu, K. Qian, Y. F. Zhang, D. L. Bao, L. F. Li, Y. Q. Wang, Z. L. Liu, J. T. Sun, T. Lei, C. Liu, J. O. Wang, K. Ibrahim, D. N. Leonard, W. Zhou, H. M. Guo, Y. L. Wang, S. X. Du, S. T. Pantelides and H. J. Gao, *Nat. Mater.*, 2017, **16**, 717–721.
- 14 L. Gao, J. T. Sun, J. C. Lu, H. Li, K. Qian, S. Zhang, Y. Y. Zhang, T. Qian, H. Ding, X. Lin, S. Du and H. J. Gao, *Adv. Mater.*, 2018, **30**, 1707055.
- 15 J. Lu, D. L. Bao, K. Qian, S. Zhang, H. Chen, X. Lin, S. X. Du and H. J. Gao, *ACS Nano*, 2017, **11**, 1689–1695.
- 16 M. M. Ugeda, A. J. Bradley, S. F. Shi, F. H. da Jornada, Y. Zhang, D. Y. Qiu, W. Ruan, S. K. Mo, Z. Hussain, Z. X. Shen, F. Wang, S. G. Louie and M. F. Crommie, *Nat. Mater.*, 2014, **13**, 1091–1095.
- 17 M. M. Ugeda, A. Pulkin, S. Tang, H. Ryu, Q. Wu, Y. Zhang, D. Wong, Z. Pedramrazi, A. Martin-Recio, Y. Chen, F. Wang, Z. X. Shen, S. K. Mo, O. V. Yazyev and M. F. Crommie, *Nat. Commun.*, 2018, **9**, 3401.
- 18 Q. Xiang, J. Yu and M. Jaroniec, *J. Am. Chem. Soc.*, 2012, **134**, 6575–6578.
- 19 T. F. Jaramillo, K. P. Jorgensen, J. Bonde, J. H. Nielsen, S. Horch and I. Chorkendorff, *Science*, 2007, **317**, 100–102.
- 20 J. Xie, H. Zhang, S. Li, R. Wang, X. Sun, M. Zhou, J. Zhou, X. W. Lou and Y. Xie, *Adv. Mater.*, 2013, **25**, 5807–5813.
- 21 X. J. Chua, J. Luxa, A. Y. S. Eng, S. M. Tan, Z. Sofer and M. Pumera, *ACS Catal.*, 2016, **6**, 5724–5734.
- 22 S. J. Rowley-Neale, J. M. Fearn, D. A. C. Brownson, G. C. Smith, X. Ji and C. E. Banks, *Nanoscale*, 2016, **8**, 14767–14777.
- 23 L. Lin, N. Miao, J. Huang, S. Zhang, Y. Zhu, D. W. Horsell, P. Ghosez, Z. Sun and D. A. Allwood, *Nano Energy*, 2017, **38**, 544–552.
- 24 G. Tang, W. Chen, X. Wan, F. Zhang and J. Xu, *Colloids Surf., A*, 2020, **587**, 124291.
- 25 Y. Wang, L. Li, W. Yao, S. Song, J. T. Sun, J. Pan, X. Ren, C. Li, E. Okunishi, Y.-Q. Wang, E. Wang, Y. Shao, Y. Y. Zhang, H.-t. Yang, E. F. Schwier, H. Iwasawa, K. Shimada, M. Taniguchi, Z. Cheng, S. Zhou, S. Du, S. J. Pennycook, S. T. Pantelides and H.-J. Gao, *Nano Lett.*, 2015, **15**, 4013–4018.
- 26 H. I. Karunadasa, E. Montalvo, Y. Sun, M. Majda, J. R. Long and C. J. Chang, *Science*, 2012, **335**, 698–702.
- 27 J. Kibsgaard, Z. Chen, B. N. Reinecke and T. F. Jaramillo, *Nat. Mater.*, 2012, **11**, 963–969.
- 28 D. Kong, H. Wang, J. J. Cha, M. Pasta, K. J. Koski, J. Yao and Y. Cui, *Nano Lett.*, 2013, **13**, 1341–1347.
- 29 G. Kresse and D. Joubert, *Phys. Rev. B: Condens. Matter Phys.*, 1999, **59**, 1758–1775.

- 30 D. Vanderbilt, *Phys. Rev. B: Condens. Matter Mater. Phys.*, 1990, **41**, 7892–7895.
- 31 G. Kresse and J. Furthmuller, *Phys. Rev. B: Condens. Matter Mater. Phys.*, 1996, **54**, 11169–11186.
- 32 J. P. Perdew, K. Burke and M. Ernzerhof, *Phys. Rev. Lett.*, 1996, **77**, 3865–3868.
- 33 J. P. Perdew, J. A. Chevary, S. H. Vosko, K. A. Jackson, M. R. Pederson, D. J. Singh and C. Fiolhais, *Phys. Rev. B: Condens. Matter Mater. Phys.*, 1992, **46**, 6671–6687.
- 34 T. Bucko, J. Hafner, S. Lebegue and J. G. Angyan, *J. Phys. Chem. A*, 2010, **114**, 11814–11824.
- 35 J. C. Lu, L. Gao, S. R. Song, H. Li, G. F. Niu, H. Chen, T. Qian, H. Ding, X. Lin, S. X. Du and H. J. Gao, *ACS Appl. Nano Mater.*, 2021, **4**, 8845–8850.
- 36 L. T. L. Lee, J. He, B. Wang, Y. Ma, K. Y. Wong, Q. Li, X. Xiao and T. Chen, *Sci. Rep.*, 2014, **4**, 4063.
- 37 M. I. B. Utama, X. Lu, D. Zhan, S. T. Ha, Y. Yuan, Z. Shen and Q. Xiong, *Nanoscale*, 2014, **6**, 12376–12382.
- 38 P. Tonndorf, R. Schmidt, P. Bottger, X. Zhang, J. Borner, A. Liebig, M. Albrecht, C. Kloc, O. Gordan, D. R. T. Zahn, S. M. de Vasconcellos and R. Bratschitsch, *Opt. Express*, 2013, **21**, 4908–4916.
- 39 Y. Wu, M. Xu, X. Chen, S. Yang, H. Wu, J. Pan and X. Xiong, *Nanoscale*, 2016, **8**, 440–450.
- 40 J. Huang, B. Jin, H. Liu, X. Li, Q. Zhang, S. Chu, R. Peng and S. Chu, *J. Mater. Chem. A*, 2018, **6**, 11424–11434.
- 41 A. Houas, H. Lachheb, M. Ksibi, E. Elaloui, C. Guillard and J.-M. Herrmann, *Appl. Catal., B*, 2001, **31**, 145–157.
- 42 Y. Zhao, J. Tu, Y. Sun, X. Hu, J. Ning, W. Wang, F. Wang, Y. Xu and L. He, *J. Phys. Chem. C*, 2018, **122**, 26570–26575.
- 43 C. Dai, E. Qing, Y. Li, Z. Zhou, C. Yang, X. Tian and Y. Wang, *Nanoscale*, 2015, **7**, 19970–19976.